

A 3D k-Space Fourier Encoding and Reconstruction Framework for Simultaneous Multi-Slab (SMSlab) Acquisition

Erpeng Dai¹, Yuhsuan Wu¹, Wenchuan Wu², Rui Guo¹, Simin Liu¹, Karla L. Miller²,
Zhe Zhang³, and Hua Guo¹

¹Center for Biomedical Imaging Research, Department of Biomedical Engineering,
School of Medicine, Tsinghua University, Beijing, China, People's Republic of,

²Wellcome Centre for Integrative Neuroimaging, FMRIB, Nuffield Department of
Clinical Neurosciences, University of Oxford, UK,

³China National Clinical Research Center for Neurological Diseases, Beijing Tiantan
Hospital, Capital Medical University, Beijing, China, People's Republic of,

Running Title: A 3D k-Space Framework for SMSlab

Word Count: ~4300

***Correspondence to:**

Hua Guo, PhD

Center for Biomedical Imaging Research

Department of Biomedical Engineering

Tsinghua University, Beijing, China

Phone: +86-10-6279-5886

Email: huaguo@tsinghua.edu.cn

Grant sponsor:

This work was supported by the National Natural Science Foundation of China
(61571258) and National Key Research and Development Program of China
(2017YFA0205904 and 2017YFC0108900).

Abstract

Purpose: To propose a novel 3D k-space Fourier encoding and reconstruction framework for simultaneous multi-slab (SMSlab) acquisition and demonstrate its efficacy in high-resolution imaging.

Methods: First it is illustrated in theory how the inter-slab gap interferes with the formation of the SMSlab 3D k-space. Then joint RF and gradient encoding are applied to remove the inter-slab-gap interference and form a SMSlab 3D k-space. In vivo experiments are performed to validate the proposed theory. Acceleration in the proposed SMSlab 3D k-space is also evaluated.

Results: High-resolution (1.0 mm isotropic) images can be reconstructed using the proposed SMSlab 3D framework. CAIPI sampling and 2D GRAPPA reconstruction can also be applied in the SMSlab 3D k-space. Compared with conventional multi-slab acquisition, SMSlab exhibits better SNR maintainability (such as lower g-factors), especially at high acceleration factors.

Conclusion: It is demonstrated that the joint application of RF and gradient encoding enables SMSlab within a 3D Fourier encoding framework. Images with high isotropic resolution can be reconstructed and further acceleration is also applicable. The proposed SMSlab 3D k-space can be valuable for both high-resolution and high-efficiency diffusion and functional MRI.

Key words: simultaneous multi-slab; 3D k-space; high-resolution; CAIPI; RF encoding

Introduction

Diffusion MRI (dMRI) and functional MRI (fMRI) are two important imaging tools for neuroscience studies (1,2). In both dMRI and fMRI, spatial resolution and scan efficiency play crucial roles (3). In dMRI, high resolution can help observe finer fiber structures, depict sharp turns at the gray-white matter boundary and detect more complex fiber architectures (4,5). In fMRI, increasing the spatial resolution can help reduce the influence of large vessels and localize the neural activity area more accurately (6). Increasing the scan speed is also very important, such as reducing the effects of subject motion. Meanwhile, in fMRI, increasing the temporal resolution can resolve physiological signal fluctuation and improve the accuracy of statistical analysis (7).

However, it is challenging to achieve high-resolution and high-efficiency dMRI and/or fMRI using the conventional 2D or 3D EPI. There are several limiting factors. Increasing the spatial resolution can degrade image signal-to-noise ratio (SNR), which is intrinsically low for dMRI. High spatial resolution also increases the sampling matrix and readout window, which may raise high requirements for gradient systems, especially when using fast switching ratios. A prolonged readout window can lead to more severe image distortion under the presence of the field inhomogeneity, especially for single-shot EPI (ss-EPI). Although multi-shot acquisitions can help increase SNRs and reduce image distortion (8-10), these methods inevitably prolong the scan time. 3D EPI acquisitions can also be used to improve SNR by exciting and encoding large FOVs in the slice direction (11,12). However, the main challenge is that the repetition time (TR) is usually too short (~ 100 ms) for a sufficient T_1 recovery in 3D EPI.

Recently, a series of hybrid 2D/3D techniques have been developed for high-resolution and high-efficiency dMRI and fMRI. These methods mainly fall into two categories: simultaneous multi-slice (SMS) (7,13,14) and 3D multi-slab (15-18). In SMS, multiple 2D slices are excited simultaneously and TR can be shortened by R_{SMS} fold compared to 2D EPI, where R_{SMS} is the number of simultaneously excited slices. Compared with traditional parallel imaging (PI) (19,20), SMS does not suffer from

$\sqrt{R_{SMS}}$ SNR loss (21). Multi-slab divides the whole acquisition into several sub-volumes and conducts a 3D encoding for each sub-volume. As a 3D acquisition method, multi-slab can partially compensate for the SNR degradation from increasing spatial resolution by exciting and encoding large FOVs in the slice direction. Meanwhile, compared with conventional 3D EPI, SMS and 3D multi-slab still have sufficient TR (≥ 1.8 s) for T_1 recovery (15,17,21) and thus can maintain a high SNR efficiency.

Numerous studies have demonstrated the success of either SMS or 3D multi-slab in dMRI and fMRI, particularly for whole-brain studies (3,4,7,22-26). However, when pushing the spatial resolution to 1 mm isotropic or higher, neither multi-slab nor SMS can guarantee an optimal SNR efficiency (15,16,24). Therefore, in this study, we aim to develop a new method to combine SMS and multi-slab to further increase the SNR efficiency. Here, simultaneous multi-slab is termed “SMSlab”, to distinguish it from conventional SMS or 3D multi-slab.

Although either SMS or multi-slab alone can be described using a 3D Fourier encoding framework (27), it is less straightforward to describe the SMSlab problem in terms of 3D k-space. The main reason is that the definitions of resolution for multi-slab and SMS are different (28). The resolution in the multi-slab acquisition is defined as the slice thickness to be reconstructed (termed “true resolution” here). However, in the SMS 3D framework, the resolution is more like a virtual concept (termed “virtual resolution ” here), which is typically referred to the center-to-center distance of two adjacent slices, rather than the slice thickness (27). When combining multi-slab and SMS, the true resolution and virtual resolution are mixed together. They are hard to be disentangled by only using gradient encoding, as there is merely one physical independent k_z dimension. A more detailed explanation will be given in the **Theory** session.

Previously, Zahneisen B et al has proposed a 4D k-space concept to address the intra- and inter-slab k_z encoding conflicts in SMSlab. In the SMSlab 4D k-space, the 3rd dimension, k_z , is used for the intra-slab encoding, which is accomplished by the k_z gradients. The 4th dimension, termed k_{SMS} , is used for the SMS encoding, which is

completed by using both the RF and gradient encoding. In this study, with the similarly basic idea, we propose a novel 3D k-space Fourier encoding and reconstruction framework for SMSlab. First, it is explained in detail how the inter-slab gap interferes the formation of a SMSlab 3D k-space. Then it is illustrated how to form a 3D k-space framework for SMSlab, by jointly using RF and gradient encoding. It is finally demonstrated that in the proposed SMSlab 3D k-space, existing sampling and reconstruction methods, such as controlled aliasing in parallel imaging (CAIPI) (29) and 2D GRAPPA (30), can also be directly applied.

Theory

In this section, we first explain why SMSlab cannot be straightforwardly represented in a 3D k-space, by only using gradient encoding. Then it is introduced how to construct a 3D k-space for SMSlab by joint RF and gradient encoding. In the following description, we use “slice” to refer to the final reconstructed z resolution and “slab” to refer to the width of the excited z extent. For clarity, a $R_{\text{SMS}}=2$ SMSlab acquisition is used as an example, while it is straightforward to extend the related theory and method to $R_{\text{SMS}}>2$ cases.

3D k_z encoding

In the traditional 3D and multi-slab acquisition (Figure 1A), k_z encoding is implemented by adding a z gradient blip in the slice direction. The k_z encoding creates a Fourier transform relationship between the k-space signal and the imaging object, i.e.,

$$d(k_z) = \sum_{z=0}^{N-1} \mu(z) \exp(-i2\pi \cdot z \cdot k_z / N), \quad [1]$$

where z and k_z are the index for the image and k-space, respectively; $d(k_z)$ is the k-space signal at k_z ; $\mu(z)$ is the image signal at location z ; N is the total number of slices to be reconstructed within a slab/volume. The impact of the k_z encoding gradient is to generate a linear phase variation along the slice direction. For example, Figure 1B plots the phase of different slices at $k_z=1$. The phase at slice z after the k_z -th gradient (defined

as θ_{z,k_z}) can be calculated as $\theta_{z,k_z} = 2\pi \cdot z \cdot k_z / N$. The meaning of the symbols are the same as Eq. [1]. Here it is assumed that slice 1 is located at the isocenter of slice encoding gradient ($z=0$).

The inter-slab gap interference

SMSlab is different from 3D acquisition in that the excited extent is not a continuous volume, i.e., a gap (d_{gap}) exists between neighboring slabs (Figure 1C). Although we can still take all excited slabs and the inter-slab gap as a whole volume and continue using a conventional 3D encoding framework for the assumed whole volume, such an encoding manner needs to acquire more k_z lines and thus time inefficient. Alternatively, we can just encode the excited slabs, as no signal is excited in the inter-slab region (assuming an ideal RF slice profile). To achieve this, the FOV in the slice direction is defined as $FOV_z = R_{\text{SMS}} \cdot N \cdot \Delta z$, where Δz is the slice thickness to be reconstructed, N is the number of slices in each slab and R_{SMS} is the number of simultaneously excited slabs. However, this can cause new problems. As the phase generated by the gradient encoding is linearly proportional to the distance away from the isocenter, the inter-slab gap (d_{gap}) will generate an extra phase on slabs that are not at the isocenter, i.e., slab 2 in Figure 1C. The amount of the extra phase can be calculated as

$$\varphi = -(2\pi \cdot d_{\text{gap}} \cdot k_z) / (R_{\text{SMS}} \cdot N \cdot \Delta z). \quad [2]$$

The corresponding phase of different slices at $k_z=1$ are plotted in Figure 1D. As shown, a phase jump of φ appears at the junction of slab 1 and 2. Now the relationship between the k-space signal and the object is rewritten as

$$d(k_z) = \sum_{z=0}^{N-1} \mu(z) \exp(-i2\pi \cdot z \cdot k_z / N) + \sum_{z=N}^{2N-1} \mu(z) \exp(i(-2\pi \cdot z \cdot k_z / N + \varphi)), \quad [3]$$

which violates the Fourier encoding condition (Eq. [1]). As such, the new 3D encoding model with the definition $FOV_z = R_{\text{SMS}} \cdot N \cdot \Delta z$ cannot be applied for SMSlab directly.

The next problem is how to remove the extra phase generated by the inter-slab gap. In addition to gradient encoding, RF encoding is another method for phase encoding.

Unlike gradient encoding, the phase from RF encoding has no direct spatial dependence (14). This may be used to remove the extra phase ϕ in Eq. [3].

The traditional SMS pulse is a sum of R_{SMS} frequency modulated RF pulses

$$RF_{SMS}(t) = \sum_{n=1}^{R_{SMS}} RF(t) \exp(i\omega_n t), \quad [4]$$

where $RF(t)$ is a single-band pulse, ω_n is the frequency modulation for slice/slab n .

If adding a phase term $-(n-1) \cdot \phi$ ($n=1, 2, 3, \dots, R_{SMS}$) to different sub-pulse n before the combination, i.e.,

$$RF_{SMS}(t) = \sum_{n=1}^{R_{SMS}} RF(t) \exp[i(\omega_n t - (n-1)\phi)], \quad [5]$$

the inter-slab gap generated phase on slab n can be cancelled out and a Fourier encoding relationship is recreated between the k-space signal and the imaging object.

Blipped-CAIPI-like off-isocenter phase

In the above session, it is assumed that the reference slice (slice 1) is at the isocenter. If not, another phase offset ψ will be generated during the gradient encoding. Unlike ϕ , ψ is the same for all slabs in SMSlab and can be removed during the reconstruction (21). Actually, this is exactly the same off-isocenter phase problem in blipped-CAIPI (21).

To illustrate the proposed SMSlab acquisition more intuitively, a schematic diagram is shown in Figure 2. Figure 2A shows a general SMSlab excitation: two excited slabs are separate and no slice is at the isocenter. The RF encoding (Eq. [5]) removes the inter-slab gap imposed phase (ϕ) and the effects can be seen as that the two excited slabs are stitched together (Figure 2B). After the off-isocenter phase (ψ) correction, the excited slabs are “drawn back” to the isocenter (Figure 2C). Finally together with the 3D Fourier encoding ($\theta_{z,kz}$), thin slices can be reconstructed (Figure 2D).

Methods

Data acquisition

In vivo brain data of four healthy subjects were acquired on a Philips 3.0T Achieva

TX MRI scanner (Philips Healthcare, Best, The Netherlands), using a 32-channel head coil. All human studies were performed under institutional review board approval from our institution and written consent was obtained before the study.

A SMSlab sequence was designed based on a 2D spin-echo EPI sequence (Figure 3A). The SMSlab RF pulse was designed by simply summing frequency-modulated pulses. As indicated in Eq. [2], the inter-slab gap imposed phase ϕ was proportional to k_z . Thus the adjusting phase in RF encoding also varied with k_z , resulting in dynamically changed RF_{SMS} shapes. Figures 3B and C display 4 sets of SMSlab excitation and refocusing RF pulses ($k_z = -10, -5, 0$ and 5 , assuming $FOV=1$ with arbitrary unit) in this study. Here all of the final composite SMSlab pulses are only amplitude modulated. The time-bandwidth product (TBWP) of the excitation and refocusing RF pulses were 8.016 and 4.400, respectively.

Fourteen slabs ($R_{SMS}=2$) were acquired to cover the whole brain. For each slab, 10 k_z planes (20% oversampling along the k_z direction) were acquired. For each k_z plane, 4-shot interleaved EPI (iEPI) was used for signal acquisition. Adjacent slabs were overlapped by 2 slices. Other main imaging parameters were: $FOV=220 \times 220 \times 112 \text{ mm}^3$, resolution= 1.0 mm^3 isotropic, partial Fourier factor=0.7 (k_y direction) and 1 (k_z direction), $TE/TR=75 \text{ ms} / 1.5 \text{ s}$, flip angle $\alpha=75^\circ$. The duration of the SMSlab excitation and refocusing pulses were 5.709 ms and 11.981 ms, respectively. First, fully-sampled SMSlab data were acquired ($R_{net}=1$, where R_{net} is the net acceleration factor). Then data were under-sampled using a CAIPI sampling pattern in the k_y - k_z plane, with $R_{net}=2$ ($R_y=2, R_z=1$) and $R_{net}=4$ ($R_y=4, R_z=1$). The under-sampling was achieved by using 1/2 and 1/4 of all shots, respectively. The corresponding sampling trajectories for each acquisition are shown in Figure 4A to 4C. The nominal acquisition time for a complete volume using SMSlab scan with $R_{net}=1, 2$ and 4 was 120 s, 60 s and 30 s, respectively. It should be noted the fully-sampled ($R_{net}=1$) SMSlab scan is only used to demonstrate the feasibility of the proposed method and does not accelerate the scan (similar to ref. (27)), as it requires R_{SMS} times of k_z encoding, when compared to encoding a single slab.

Traditional 3D multi-slab data were also acquired for comparison, with TE/TR=57 ms / 3.0 s, flip angle $\alpha=90^\circ$. The duration of the multi-slab excitation and refocusing pulses were 2.854 ms and 5.984 ms, respectively. Other imaging parameters were the same as SMSlab, except for the RF pulse shapes. Then data were also under-sampled using a CAIPI sampling pattern in the k_y - k_z plane. Two net acceleration factors were tested, $R_{\text{net}}=2$ ($R_y=2$, $R_z=1$) and $R_{\text{net}}=4$ ($R_y=4$, $R_z=1$). The corresponding sampling trajectories for each acquisition are shown in Figure 4D to 4F. The nominal acquisition time for a complete volume using traditional multi-slab scan with $R_{\text{net}}=1$, 2 and 4 was 120 s, 60 s and 30 s, respectively. From Figure 4, it can be seen that using the proposed SMSlab pulse, SMSlab generates the same 3D k-space shape as the traditional multi-slab acquisition, but with different definition of Δk_z .

As mentioned above, SMSlab has a much longer TE (75 ms) than multi-slab (57 ms). In this study, we termed this as the “unequal TE case”. In the following sessions, unless otherwise specified, the results were from the unequal TE case. The reason was that only the basic multiband pulse design (frequency modulation and sum) was implemented for SMSlab, which has a relatively long pulse duration and thus causes a longer TE. This may degrade the SNR performance of SMSlab, when compared with the multi-slab acquisition. To make a fair SNR comparison between SMSlab and multi-slab, we conducted another experiment, in which the TE of multi-slab was manually prolonged to the same value of SMSlab, i.e. 75 ms. This new experiment was termed as the “equal TE case”.

Calibration scan

Two calibration scans were conducted in this study, to estimate the coil sensitivity map and the slice profile, respectively. 2D 4-shot iEPI was used to estimate the coil sensitivity map, with image resolution $1 \times 1 \times 2 \text{ mm}^3$. The reason for not using a 3D multi-slab acquisition was to avoid the influence of the slab boundary artifacts. The resolution of the sensitivity calibration scan was first interpolated to the target resolution in the slice direction. Then the reference data for PI reconstruction was generated by extracting the data at the corresponding SMSlab excited locations.

The calibration scan for the slice profile was conducted using the same sequence as the actual scan, but with 2-fold oversampling along the slice direction for each slab. To save the scan time, 2-shot iEPI was used to acquire each k_z plane and the resolution is $2 \times 2 \times 1 \text{ mm}^3$. The TR of the calibration scan for the slice profile was kept the same as the actual scan. The calibration images were first interpolated to the normal imaging resolution ($1 \times 1 \times 1 \text{ mm}^3$). Then the slice profiles were calculated as described in ref. (17).

Reconstruction

First, blipped-CAIPI-like off-isocenter phase (ψ) was corrected, as described in ref. (21). Then Nyquist N/2 ghost artifacts were corrected using a singular value decomposition (SVD) based algorithm (31). The $k_z=0$ data were used to search for the optimal constant and linear phase for ghost correction. This calculated phase information was applied to all other k_z planes. Before the reconstruction, data were first compressed to 8 channels using the geometric-decomposition coil compression (GCC) algorithm (32).

For the under-sampled image data, 2D GRAPPA (30) was used to recover the missing data. The kernel size was $5 \times 7 \times 3$ ($k_x \times k_y \times k_z$), with standard Tikhonov regularization $\lambda=0.075$ applied in the weight fitting process. For both fully-sampled and GRAPPA-recovered data, partial Fourier reconstruction was conducted in k_y direction using a POCS-based method (33). Finally, the resultant data were inverse Fourier transformed and complex averaged among different channels.

Another challenge in 3D multi-slab acquisition is the slab boundary artifacts, which are caused by the non-ideal RF pulse profiles (16-18). The slab boundary artifacts mainly include the decreased signal intensity at the slab edge, cross-talk between neighboring slabs and aliasing artifacts. In this study, nonlinear inversion for slab profile encoding (NPEN) (17) was used to correct for the slab boundary artifacts. For conventional multi-slab imaging, the original NPEN reconstruction can be formulated as

$$E(\mathbf{x}) = \mathbf{d}, \mathbf{x} = [\boldsymbol{\mu}, \mathbf{S}]^T, \quad [6]$$

$$E(\mathbf{x}) = (\mathbf{PFCs}_1\boldsymbol{\mu} \quad \mathbf{PFCs}_2\boldsymbol{\mu} \quad \dots \quad \mathbf{PFCs}_{N_{\text{slab}}}\boldsymbol{\mu}), \quad [7]$$

where $\boldsymbol{\mu}$ is the image to be reconstructed, $\mathbf{S} = [\mathbf{s}_1 \quad \mathbf{s}_2 \quad \dots \quad \mathbf{s}_{N_{\text{slab}}}]^T$ is the RF pulse slice profile of different slabs, $\mathbf{d} = [\mathbf{d}_1 \quad \mathbf{d}_2 \quad \dots \quad \mathbf{d}_{N_{\text{slab}}}]^T$ is the acquired k-space signal, E is the nonlinear encoding matrix, including: the coil sensitivity \mathbf{C} , Fourier transform operator \mathbf{F} , and the operator to select the sampled k-space locations \mathbf{P} .

In SMSlab, the aliasing patterns have changed from intra-slab aliasing to inter-slab aliasing (Figure 5). Hence, the NPEN algorithm is refined and the new encoding matrix can be written as

$$E(\mathbf{x}) = (\mathbf{P}\hat{\mathbf{F}}\mathbf{C}\hat{\mathbf{s}}_1\boldsymbol{\mu} \quad \mathbf{P}\hat{\mathbf{F}}\mathbf{C}\hat{\mathbf{s}}_2\boldsymbol{\mu} \quad \dots \quad \mathbf{P}\hat{\mathbf{F}}\mathbf{C}\hat{\mathbf{s}}_{N_{\text{slab}}/R_{\text{SMS}}}\boldsymbol{\mu}). \quad [8]$$

Two main changes are made here. $\hat{\mathbf{s}}_j$ is the slice profile of the j -th SMSlab pulse and $\hat{\mathbf{F}}$ here means the Fourier transform operator over the stitched slabs (Figure 2C), rather than the whole volumes. The NPEN reconstruction procedures and constraints were the same as ref. (17), with the regularization parameters $\alpha=0.2$ and $\beta=0.4$.

Two methods were used to compare the SNR performance of SMSlab and the 3D multi-slab acquisitions. First, to assess the SNR changes and distributions over the whole volume, temporal SNR (tSNR) was calculated. The third subject underwent a scan with 10 repetitions, using both the 3D multi-slab and SMSlab acquisitions. Then tSNR was calculated as $tSNR = \bar{\mu} / \sigma$, where $\bar{\mu}$ and σ were the mean signal and the standard deviation of the signal over time, respectively.

Additionally, to assess the SNR maintainability under different acceleration factors, the g-factor maps of different acquisitions were calculated using the pseudo-multiple replica method with 128 repetitions (34). However, non-linear operations in the partial Fourier reconstruction and the NPEN correction violates the requirements of the pseudo-multiple replica method. As such, the reconstruction was refined from two aspects in this step. First, the POCS-based partial Fourier reconstruction was replaced by zero filling. Second, no NPEN correction was conducted and only the central slice

of each slab (slice 5) were selected for comparison, to avoid the influence of the slab boundary artifacts.

Results

Figure 6A shows the direct inverse FFT reconstruction of the fully-sampled 3D k-space from two simultaneously excited slabs, using a conventional SMS pulse without RF encoding (Eq. [4]). For each slab, only one central and outer slices (slice 5 and 10) are displayed. As shown in results, using the traditional SMS pulse, the inter-slab gap added linear increased phase ϕ to slab 2 at different k_z planes. As ϕ is proportional to k_z (Eq. [2]), this linear phase increment leads to a shift of the reconstructed images along the slice direction. The shifted images are further folded with slices from slab 1, causing abnormal aliasing artifacts. The amount of shift is determined by the ratio between the inter-slab gap d_{gap} and the defined $FOV_z = R_{\text{SMS}} \cdot N \cdot \Delta z$. Figure 6B shows the results using the proposed SMSlab pulse with RF encoding (Eq. [5]). As shown in Figure 6B, thin slices can be well reconstructed for both slabs and the aliasing artifacts only appear at the slab boundaries (yellow arrowheads). The signal degradation from the center to the edge can also be observed, which is mainly due to non-ideal RF pulse slice profile. After the modified NPEN reconstruction, slab boundary artifacts (both aliasing artifacts and signal decay) are well corrected, as shown in Figure 6C. The whole images of each slab are shown in Supporting Information Figure s1. From Figure s1 A, it can be seen that the rightmost 6 slices in slab 2 are shifted to slab 1, when using the conventional SMS pulse.

Figure 7 shows the results of the second subject in the sagittal view, without and with NPEN correction. Three different SMSlab acquisitions are included: (A) fully-sampled acquisition; (B) $R_{\text{net}}=2$ with CAIPI; and (C) $R_{\text{net}}=4$ with CAIPI. It can be seen that using the refined NPEN correction, all slices can be well reconstructed and the boundary artifacts can be significantly suppressed, though not fully removed. The similar results are also observed in the coronal view, as shown in Supporting

Information Figure S2. Compared with the fully-sampled data, the two accelerated acquisitions show different levels of SNR loss.

Figure 8 compares the NPEN corrected images and tSNR maps changes from the slab center to the edge. Three different SMSlab acquisitions are included: $R_{\text{net}}=1, 2$ and 4. Only slight tSNR differences are observed when comparing the slab center and edge. However, as shown in Figure 7, the two accelerated acquisitions show different levels of tSNR loss, compared with the fully-sampled data.

Figure 9 shows the tSNR comparison between the 3D multi-slab and the SMSlab acquisition in the unequal TE case, with different acceleration factors. The multi-slab and SMSlab results are shown on the left and right panels, respectively. In general, the tSNR of the SMSlab acquisition is lower than the 3D multi-slab acquisition, at the same acceleration factor. The reason should be the prolonged TE in the SMSlab acquisition (57 ms in multi-slab vs. 75 ms in SMSlab), which will be further illustrated in the discussion parts. However, in the equal TE case, SMSlab shows higher tSNRs than multi-slab, as shown in Supporting Information Figures S3. It should also be noted that in the equal TE case, SMSlab at $R_{\text{net}}=2$ still shows comparable tSNRs than fully-sampled multi-slab ($R_{\text{net}}=1$), but only takes half of the scan time.

The SNR maintainability of SMSlab is further demonstrated by the g-factor maps, as shown in Figure 10. As slab boundary artifacts cannot be removed during the g-factor calculation, we only show the central slice of one slab here. It can be seen that in both the unequal and equal TE case, SMSlab outperforms the multi-slab acquisition by showing lower g-factors, especially when $R_{\text{net}}=4$.

Discussion

Multi-slab acquisition has been used as an important technique in high-resolution dMRI and fMRI studies. It can be combined with SMS to further improve the scan efficiency and SNR efficiency. However, the fact that the intra-slab and inter-slab slices share the same physical z axis hinders the direct Fourier encoding of SMSlab. In this study, we demonstrated that by using joint RF and gradient encoding, a 3D Fourier encoding and

reconstruction framework can be formed for SMSlab. As such, existing methods for 3D reconstruction, such as CAIPI and 2D GRAPPA, can be used in the proposed SMSlab 3D framework directly.

In the theory parts, we have mentioned that SMSlab generally cannot be encoded by only using k_z gradients. However, there is an exception when the ratio between the inter-slab gap (d_{gap}) and the defined FOV of SMSlab ($R_{\text{SMS}}N\Delta z$) is an integer. In this case the inter-slab-gap generated phase ϕ will also be integer times of 2π , which will actually have no impacts on the k_z encoding and thus make the proposed RF encoding unnecessary. This has been demonstrated in several studies (35-37). However, in SMSlab acquisitions, slab oversampling and overlap are needed for slab boundary artifact correction, making the ability of flexibly defining d_{gap} and $R_{\text{SMS}}N\Delta z$ desirable. In this study, we proposed a generalized framework for SMSlab acquisition that is independent of the ratio between d_{gap} and $R_{\text{SMS}}N\Delta z$. It is also worth noting that the inter-slab gap generated phase is different from blipped-CAIP-like off-isocenter phase. The latter is identical for all slices / slabs and can be removed in the reconstruction step, while the inter-slab gap generated phase varies for different slabs and cannot be removed in the reconstruction step.

Slab boundary artifacts are a common problem for both the conventional multi-slab and SMSlab acquisition. In this study, NPEN is modified to correct for the slab boundary artifacts. This can suppress most of the artifacts in SMSlab (Figure 7 and Supporting Information Figure S2). However, some residual slab boundary artifacts can still be observed in SMSlab, which are more obvious than multi-slab (Figure 9 and Supporting Information Figure S3). The reason might be that the aliasing patterns in SMSlab are more complex than multi-slab, i.e. from intra-slab aliasing to inter-slab aliasing (Figure 5). In multi-slab, the intra-slab aliasing means that the “true slices” and “aliased slices” at one location come from the same slab and use similar coil sensitivity information. The inter-slab aliasing in SMSlab means that the “true slices” and the “aliasing slices” at the same location now are encoded with much more different coil sensitivity information, which may make the PI reconstruction and slab boundary

correction more difficult. In the future, integrating the slab boundary artifact correction into the PI reconstruction can be considered to improve the performance.

As demonstrated in this work, SMSlab can also be integrated with further in-plane acceleration. However, acceleration generally degrades the SNR and thus the capacity to maintain SNR is critical for any acceleration methods. Compared with the conventional multi-slab acquisition, SMSlab has shown lower g-factors (Figure 10), particularly at high acceleration factors ($R_{\text{net}}=4$), indicating a better capacity to maintain SNR. However, this advantage is not obviously reflected in the tSNR maps from the unequal TE case (Figure 8 and 9). The main reason is that tSNR is not only related to g-factor, but also related to the intrinsic image intensity. The multi-slab protocol in this study has a shorter TE and longer TR than the SMSlab protocol (57 ms in multi-slab vs. 75 ms in SMSlab), generating an intrinsically higher signal intensity and thus higher tSNR. When manually setting the TEs of SMSlab and multi-slab to the same, SMSlab shows higher tSNRs than multi-slab (Supporting Information Figure S3). The mathematical derivation of SNR difference caused by different TEs is given in appendix 1.

Combination of multi-slab and SMS has also been demonstrated in SLIDER (38-40), where high resolution is achieved by “super-resolution” reconstruction (38,39) and RF encoding (40), rather than the k_z gradient encoding in the conventional multi-slab and SMSlab. Therefore, SLIDER is not affected by the inter-slab gap interference discussed in this work. However, the performance of SLIDER might be affected by the fidelity of the RF pulse. For certain MRI scanners, further evaluations are needed to determine which technique, multi-slab or SLIDER, is more preferable.

In this preliminary study, the feasibility of the proposed SMSlab 3D k-space has been demonstrated. However, there are still some limitations. First, the design of the SMSlab RF pulse needs further optimization. The RF pulse is crucial for SMSlab acquisition and the current pulse generates quite long TE, which degrades the SNR performance of SMSlab, as shown above. Advanced RF pulse design (41-44) should be considered to shorten TE and increase the image SNRs. Such an improvement may

further allow higher acceleration factors. Second, it's observed that when using $R_{\text{net}}=4$, both multi-slab and SMSlab show an obvious SNR degradation. Advanced reconstruction algorithms, such as SPIRiT (45) and virtual coil concept (46), can be used to boost SNR in the future. Third, when applying SMSlab to diffusion weighted images, physiological motion can cause phase variations among different shots (47). Additional phase correction methods, including navigator acquisition (48,49) and reconstruction algorithms (8,10,23,36,50), would be necessary for dMRI. Finally, the results presented here utilized spin echo EPI (SE-EPI) only. However, there should be no obstacles to extend the proposed acquisition and reconstruction method to gradient echo EPI (GRE-EPI), as appropriate for fMRI.

Conclusion

In conclusion, it is demonstrated that the joint application of RF and gradient encoding enables SMSlab within a 3D Fourier encoding framework. High-resolution isotropic images (1.0 mm isotropic) can be obtained with the proposed method and further acceleration can also be applied. The resulting methods potentially benefit both high-resolution dMRI and fMRI.

Acknowledgements

The author would like to thank Drs. Sjoerd Crijns, Hui Wang and Arthur Felipe from Philips Healthcare for helpful discussions about the implementation of dynamically changed RF pulse shapes. This work was supported by the National Natural Science Foundation of China (61571258) and National Key Research and Development Program of China (2017YFA0205904 and 2017YFC0108900).

Appendix

According to the Bloch equation, the signal of spoiled SE-EPI at TE can be described as

$$S = M_0 \sin(\alpha) \exp(-TE/T_2) \left[1 - 2 \exp(-(TR - TE/2)/T_1) + \exp(-TR/T_1) \right] / \left[1 + \cos(\alpha) \exp(-TR/T_1) \right], \quad [\text{A1}]$$

where M_0 is the equilibrium longitudinal magnetization and α is the flip angle (51).

On a 3T scanner, $T_1=840$ ms and $T_2=70$ ms are assumed for white matter (52). If we further assume $M_0=1$ and use the imaging parameters in this study (multi-slab: TE=57 ms, TR=3.0 s; SMSlab: TE=75 ms, TR=1.5 s), the intrinsic signal intensities for 3D multi-slab and SMSlab are 0.43 and 0.26, respectively. Since the FOV_z of SMSlab is 2-fold of 3D multi-slab, the SNR ratio between 3D multi-slab and SMSlab is

$$SNR_{\text{multi-slab}} / SNR_{\text{SMSlab}} = S_{\text{multi-slab}} / S_{\text{SMSlab}} / \sqrt{2} = 1.17, \quad [\text{A2}]$$

with assuming equal background noise levels for the 3D multi-slab and SMSlab acquisitions. Since g-factors for 3D multi-slab and SMSlab are similar when using a lower R_{net} , thus 3D multi-slab may show similar or even higher SNR than SMSlab. Using a shorter TE, such as by delicate design of the SMSlab pulses, can boost the SNR of the SMSlab acquisition.

References

1. Van Essen DC, Ugurbil K, Auerbach E, et al. The Human Connectome Project: a data acquisition perspective. *Neuroimage* 2012;62(4):2222-2231.
2. Miller KL, Alfaro-Almagro F, Bangerter NK, et al. Multimodal population brain imaging in the UK Biobank prospective epidemiological study. *Nat Neurosci* 2016;19(11):1523-1536.
3. Setsompop K, Kimmlingen R, Eberlein E, et al. Pushing the limits of in vivo diffusion MRI for the human connectome project. *Neuroimage* 2013;80:220-233.
4. Miller KL, Stagg CJ, Douaud G, et al. Diffusion imaging of whole, post-mortem human brains on a clinical MRI scanner. *Neuroimage* 2011;57(1):167-181.
5. Sotiropoulos SN, Jbabdi S, Xu J, et al. Advances in diffusion MRI acquisition and processing in the Human Connectome Project. *Neuroimage* 2013;80:125-143.
6. Ugurbil K, Xu J, Auerbach EJ, et al. Pushing spatial and temporal resolution for functional and diffusion MRI in the Human Connectome Project. *Neuroimage* 2013;80:80-104.
7. Feinberg DA, Setsompop K. Ultra-fast MRI of the human brain with simultaneous multi-slice imaging. *J Magn Reson* 2013;229:90-100.
8. Chen NK, Guidon A, Chang HC, Song AW. A robust multi-shot scan strategy for high-resolution diffusion weighted MRI enabled by multiplexed sensitivity-encoding (MUSE). *Neuroimage* 2013;72:41-47.
9. Porter DA, Heidemann RM. High resolution diffusion-weighted imaging using readout-segmented echo-planar imaging, parallel imaging and a two-dimensional navigator-based reacquisition. *Magn Reson Med* 2009;62(2):468-475.
10. Ma X, Zhang Z, Dai E, Guo H. Improved multi-shot diffusion imaging using GRAPPA with a compact kernel. *Neuroimage* 2016;138:88-99.
11. Mansfield P, Howseman AM, Ordidge RJ. Volumar Imaging Using Nmr Spin Echoes - Echo-Volumar Imaging (Evi) at 0.1-T. *J Phys E Sci Instrum* 1989;22(5):324-330.
12. Song AW, Wong EC, Hyde JS. Echo-volume imaging. *Magn Reson Med* 1994;32(5):668-671.
13. Larkman DJ, Hajnal JV, Herlihy AH, Coutts GA, Young IR, Ehnholm G. Use of multicoil arrays for separation of signal from multiple slices simultaneously excited. *J Magn Reson Imaging* 2001;13(2):313-317.
14. Barth M, Breuer F, Koopmans PJ, Norris DG, Poser BA. Simultaneous multislice (SMS) imaging techniques. *Magn Reson Med* 2016;75(1):63-81.
15. Frost R, Miller KL, Tijssen RH, Porter DA, Jezzard P. 3D multi-slab diffusion-weighted readout-segmented EPI with real-time cardiac-reordered K-space acquisition. *Magn Reson Med* 2014;72(6):1565-1579.
16. Van AT, Aksoy M, Holdsworth SJ, Kopeinigg D, Vos SB, Bammer R. Slab profile encoding (PEN) for minimizing slab boundary artifact in three-dimensional diffusion-weighted multislabs acquisition. *Magn Reson Med* 2015;73(2):605-613.
17. Wu W, Koopmans PJ, Frost R, Miller KL. Reducing slab boundary artifacts in three-dimensional multislabs diffusion MRI using nonlinear inversion for slab profile encoding (NPEN). *Magn Reson Med* 2016;76(4):1183-1195.
18. Engstrom M, Skare S. Diffusion-weighted 3D multislabs echo planar imaging for high signal-to-noise ratio efficiency and isotropic image resolution. *Magn Reson Med* 2013;70(6):1507-1514.
19. Pruessmann KP, Weiger M, Scheidegger MB, Boesiger P. SENSE: Sensitivity encoding for fast

- MRI. *Magn Reson Med* 1999;42(5):952-962.
20. Griswold MA, Jakob PM, Heidemann RM, et al. Generalized autocalibrating partially parallel acquisitions (GRAPPA). *Magn Reson Med* 2002;47(6):1202-1210.
 21. Setsompop K, Gagoski BA, Polimeni JR, Witzel T, Wedeen VJ, Wald LL. Blipped-controlled aliasing in parallel imaging for simultaneous multislice echo planar imaging with reduced g-factor penalty. *Magn Reson Med* 2012;67(5):1210-1224.
 22. Setsompop K, Feinberg DA, Polimeni JR. Rapid brain MRI acquisition techniques at ultra-high fields. *NMR Biomed* 2016;29(9):1198-1221.
 23. Wu W, Poser BA, Douaud G, et al. High-resolution diffusion MRI at 7T using a three-dimensional multi-slab acquisition. *Neuroimage* 2016;143:1-14.
 24. Chang H-C, Sundman M, Petit L, et al. Human brain diffusion tensor imaging at submillimeter isotropic resolution on a 3 Tesla clinical MRI scanner. *Neuroimage* 2015;118:667-675.
 25. Posse S, Ackley E, Mutihac R, et al. High-speed real-time resting-state fMRI using multi-slab echo-volumar imaging. *Front Hum Neurosci* 2013;7.
 26. Posse S, Ackley E, Mutihac R, et al. Enhancement of temporal resolution and BOLD sensitivity in real-time fMRI using multi-slab echo-volumar imaging. *Neuroimage* 2012;61(1):115-130.
 27. Zahneisen B, Poser BA, Ernst T, Stenger VA. Three-dimensional Fourier encoding of simultaneously excited slices: generalized acquisition and reconstruction framework. *Magn Reson Med* 2014;71(6):2071-2081.
 28. Zahneisen B, Aksoy M, Maclaren J, Wuerslin C, Bammer R. RF-encoding for simultaneous multi slab imaging. In *Proceedings of the 24th Annual Meeting of ISMRM, Singapore, 2016*. Abstract 3257.
 29. Breuer FA, Blaimer M, Mueller MF, et al. Controlled aliasing in volumetric parallel imaging (2D CAIPIRINHA). *Magn Reson Med* 2006;55(3):549-556.
 30. Blaimer M, Breuer FA, Mueller M, et al. 2D-GRAPPA-operator for faster 3D parallel MRI. *Magn Reson Med* 2006;56(6):1359-1364.
 31. Peterson E, Aksoy M, MacKinley J, Bammer R. Acquisition-free Nyquist ghost correction for parallel imaging accelerated EPI. In *Proceedings of the 23rd Annual Meeting of ISMRM, Toronto, Canada, 2015*. Abstract 75.
 32. Zhang T, Pauly JM, Vasanawala SS, Lustig M. Coil compression for accelerated imaging with Cartesian sampling. *Magn Reson Med* 2013;69(2):571-582.
 33. Haacke EM, Lindskog ED, Lin W. A fast, iterative, partial-Fourier technique capable of local phase recovery. *J Magn Reson* 1991;92(1):126-145.
 34. Robson PM, Grant AK, Madhuranthakam AJ, Lattanzi R, Sodickson DK, McKenzie CA. Comprehensive quantification of signal-to-noise ratio and g-factor for image-based and k-space-based parallel imaging reconstructions. *Magn Reson Med* 2008;60(4):895-907.
 35. Frost R, Jezzard P, Porter DA, Tjissen R, Miller K. Simultaneous multi-slab acquisition in 3D multi-slab diffusion-weighted readout-segmented echo-planar imaging. In *Proceedings of the 21st Annual Meeting of ISMRM, Salt Lake City, Utah, USA, 2013*. Abstract 3176.
 36. Bruce IP, Chang HC, Petty C, Chen NK, Song AW. 3D-MB-MUSE: A robust 3D multi-slab, multi-band and multi-shot reconstruction approach for ultrahigh resolution diffusion MRI. *Neuroimage* 2017;159:46-56.
 37. Chen L, Feinberg D. Simultaneous Multi-Slab Echo Volume Imaging: Comparison in Sub-Second fMRI. In *Proceedings of the 21st Annual Meeting of ISMRM, Salt Lake City, Utah,*

- USA, 2013. Abstract 0303.
38. Setsompop K, Bilgic B, Nummenmaa A, et al. Slice dithered enhanced resolution simultaneous multislice (SLIDER-SMS) for high resolution (700 μ m) diffusion imaging of the human brain. In Proceedings of the 23rd Annual Meeting of ISMRM, Toronto, Canada, 2015. Abstract 0339.
 39. Vu AT, Beckett A, Setsompop K, Feinberg DA. Evaluation of slice dithered enhanced resolution simultaneous multislice (SLIDER-SMS) for human fMRI. *Neuroimage* 2018;164:164-171.
 40. Setsompop K, Fan Q, Stockmann J, et al. High-resolution in vivo diffusion imaging of the human brain with generalized slice dithered enhanced resolution: Simultaneous multislice (gSlider-SMS). *Magn Reson Med* 2018;79(1):141-151.
 41. Pauly J, Le Roux P, Nishimura D, Macovski A. Parameter relations for the Shinnar-Le Roux selective excitation pulse design algorithm [NMR imaging]. *IEEE Trans Med Imaging* 1991;10(1):53-65.
 42. Sharma A, Lustig M, Grissom WA. Root-Flipped Multiband Refocusing Pulses. *Magn Reson Med* 2016;75(1):227-237.
 43. Norris DG, Koopmans PJ, Boyacıoğlu R, Barth M. Power independent of number of slices (PINS) radiofrequency pulses for low - power simultaneous multislice excitation. *Magn Reson Med* 2011;66(5):1234-1240.
 44. Conolly S, Nishimura D, Macovski A, Glover G. Variable-Rate Selective Excitation. *J Magn Reson* 1988;78(3):440-458.
 45. Lustig M, Pauly JM. SPIRiT: Iterative self - consistent parallel imaging reconstruction from arbitrary k - space. *Magn Reson Med* 2010;64(2):457-471.
 46. Blaimer M, Gutberlet M, Kellman P, Breuer FA, Köstler H, Griswold MA. Virtual coil concept for improved parallel MRI employing conjugate symmetric signals. *Magn Reson Med* 2009;61(1):93-102.
 47. Miller KL, Pauly JM. Nonlinear phase correction for navigated diffusion imaging. *Magn Reson Med* 2003;50(2):343-353.
 48. Jeong HK, Gore JC, Anderson AW. High-resolution human diffusion tensor imaging using 2-D navigated multishot SENSE EPI at 7 T. *Magn Reson Med* 2013;69(3):793-802.
 49. Dai E, Zhang Z, Ma X, et al. The effects of navigator distortion and noise level on interleaved EPI DWI reconstruction: a comparison between image- and k-space-based method. *Magn Reson Med* 2018;80(5):2024-2032.
 50. Chang HC, Hui ES, Chiu PW, Liu X, Chen NK. Phase correction for three-dimensional (3D) diffusion-weighted interleaved EPI using 3D multiplexed sensitivity encoding and reconstruction (3D-MUSER). *Magn Reson Med* 2018;79(5):2702-2712.
 51. Bernstein MA, King KF, Zhou XJ. CHAPTER 14.3 - RADIOFREQUENCY SPIN ECHO. *Handbook of MRI Pulse Sequences*. Burlington: Academic Press; 2004. p 630-647.
 52. Wansapura JP, Holland SK, Dunn RS, Ball WS. NMR relaxation times in the human brain at 3.0 tesla. *Jmri-J Magn Reson Im* 1999;9(4):531-538.

Figure Captions

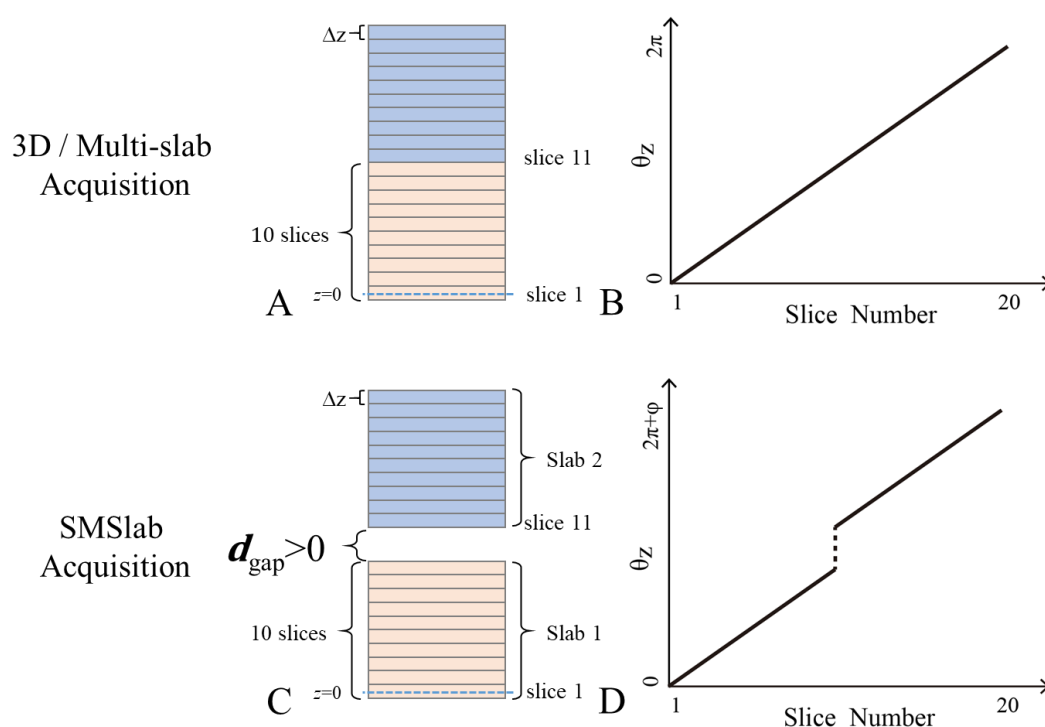


FIGURE 1. (A) and (B) The imaging diagram and phase increment along different slices at $k_z=1$ for 3D / multi-slab acquisition. (C) and (D) The imaging diagram and phase increment along different slices at $k_z=1$ for simultaneous multi-slab (SMSlab) acquisition. 10 slices are reconstructed from each slab. The inter-slab gap causes a phase jump at the junction of slab 1 and 2. For simplicity, it's assumed that slice 1 in slab 1 is at the isocenter.

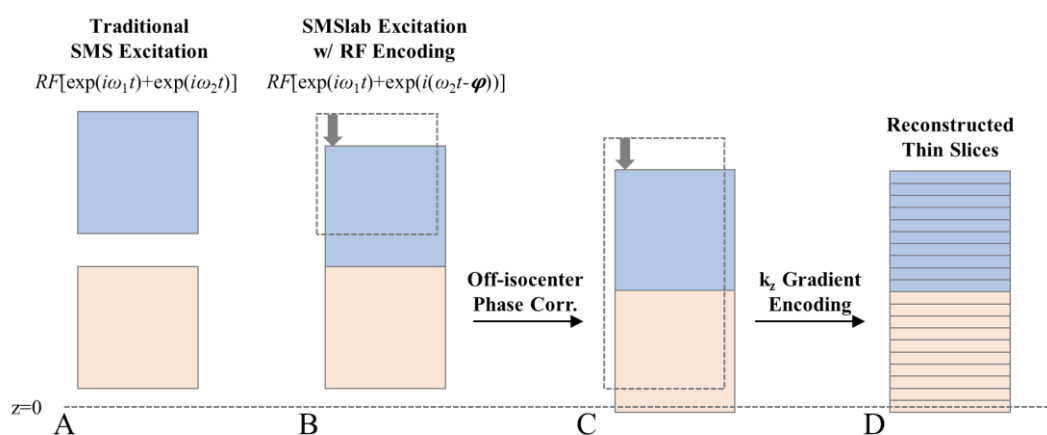


FIGURE 2. An overall diagram about the transformation of an SMSlab acquisition to the reconstructed thin slices. (A) The original slab locations using the traditional SMSslab excitation without RF encoding. (B) The equivalent slab locations using the

proposed SMSlab excitation with RF encoding. (C) The equivalent slab locations with further off-isocenter phase correction. (D) The reconstructed thin slices with k_z gradient encoding. The dashed box indicates the slab location of last step.

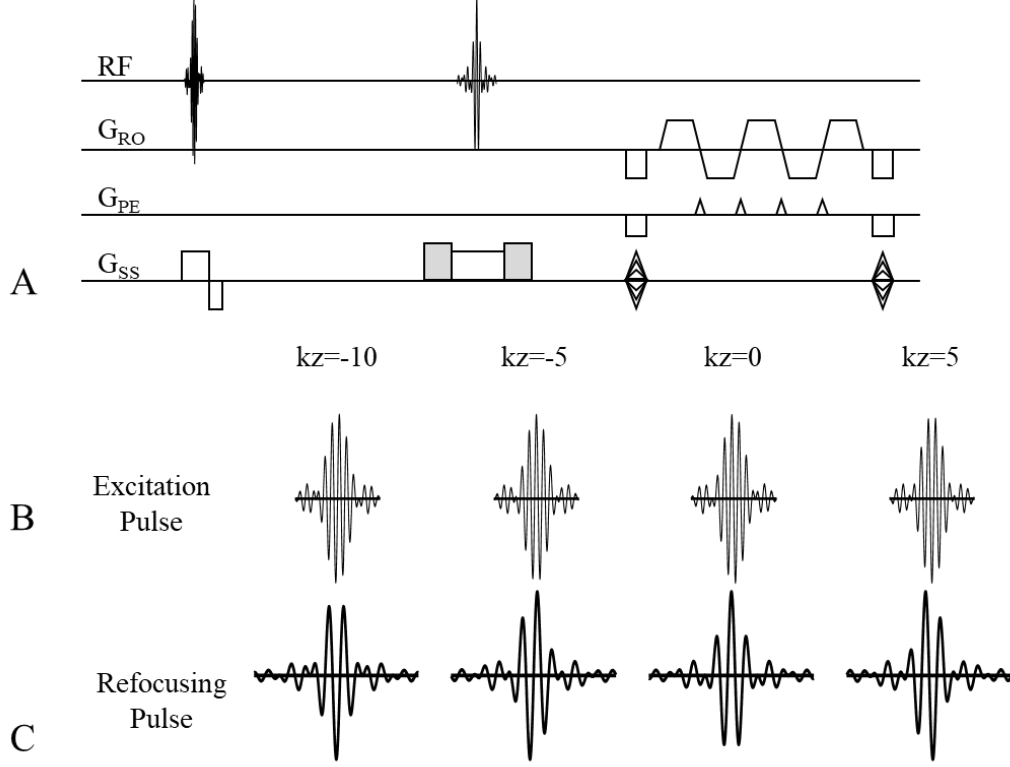


FIGURE 3. (A) The sequence diagram for the SMSlab acquisition, modified from a 2D EPI sequence. (B) and (C) Four different RF excitation and refocusing pulse sets for different k_z planes ($k_z = -10, -5, 0$ and 5 , assuming $FOV=1$ with arbitrary unit) are shown for demonstration. It should be noted the multiband pulses are only magnitude modulated.

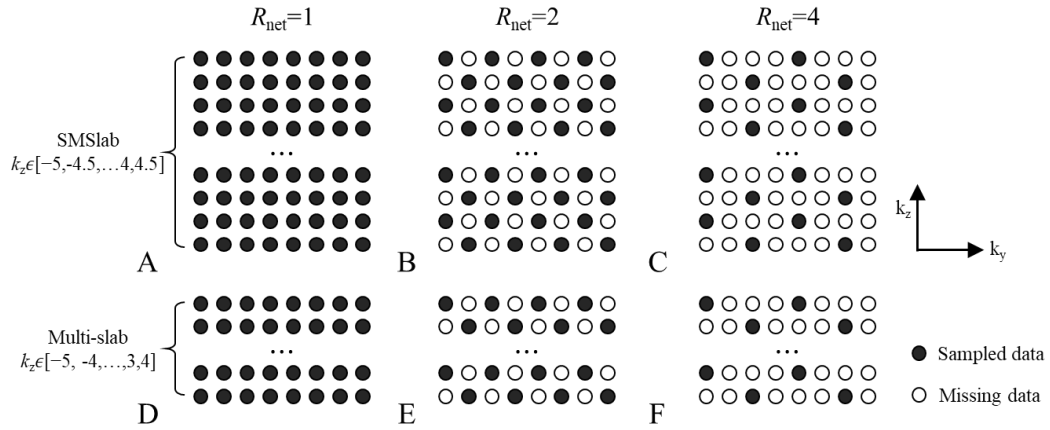


FIGURE 4. (A) to (C) The sampling trajectories for the SMSlab ($R_{SMS}=2$) acquisition

with $R_{\text{net}}=1, 2$ and 4 , respectively. (D) to (F) The sampling trajectories for the multi-slab acquisition with $R_{\text{net}}=1, 2$ and 4 , respectively. CAIPI is used for $R_{\text{net}}>1$ data. Using the proposed SMSlab pulse, SMSlab generates the same 3D k-space shape as the traditional multi-slab acquisition, but with different definition of Δk_z .

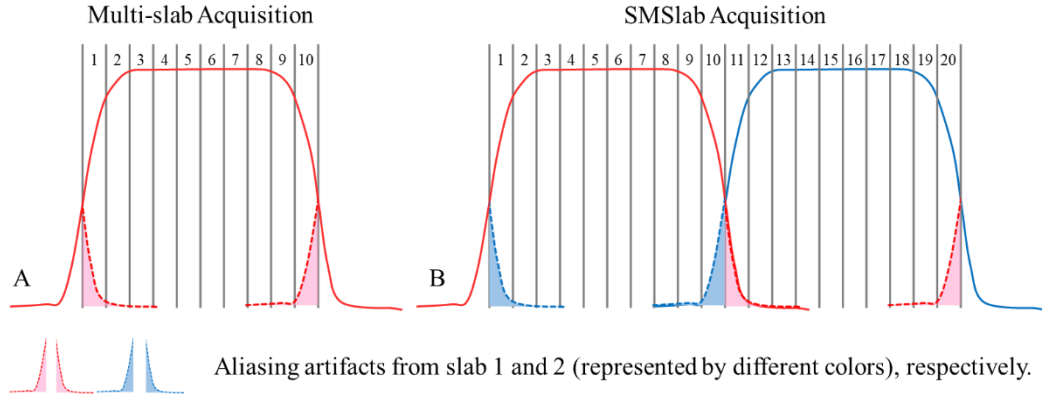
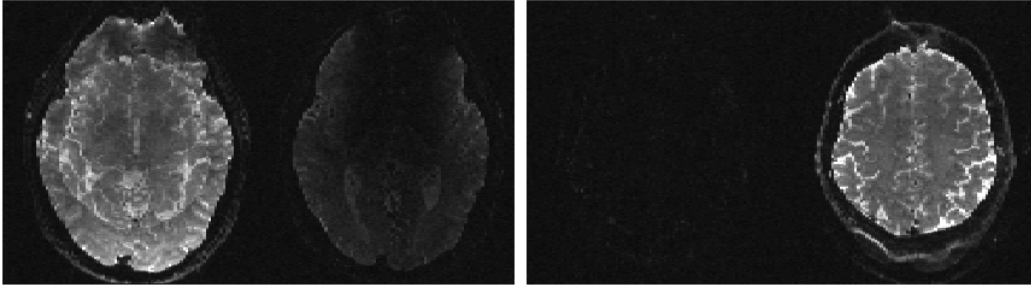
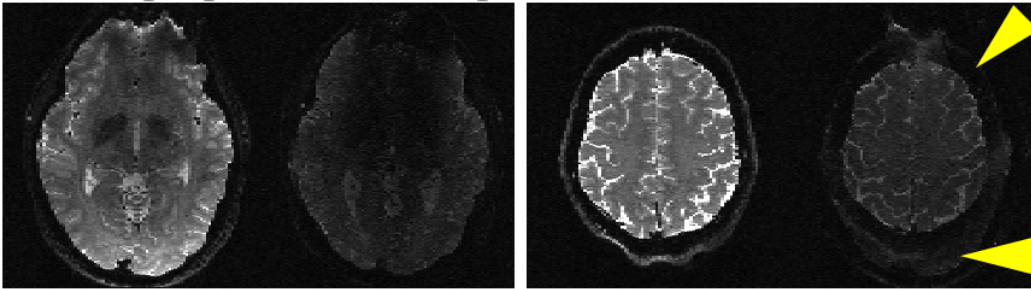


FIGURE 5. The slab boundary aliasing artifacts for multi-slab acquisition (A) and SMSlab (B). Different colors represent aliasing from different slabs. It is noteworthy that for SMSlab, the aliasing pattern changes from intra-slab aliasing to inter-slab aliasing.

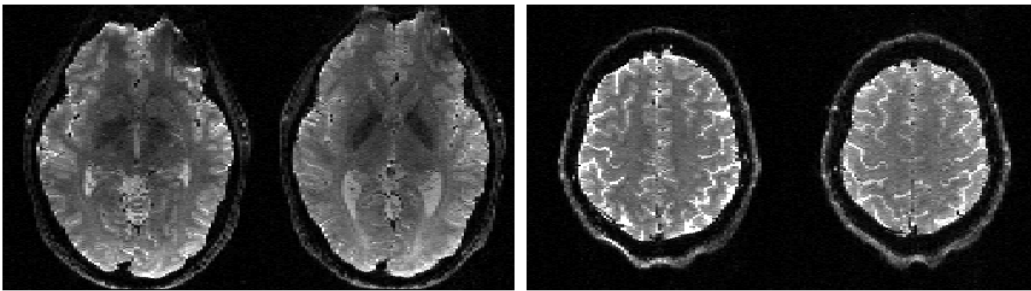
A. Traditional SMS pulse



B. The proposed SMSlab pulse



C. The proposed SMSlab pulse + NPEN correction



Slab 1, Slice 5 Slab 1, Slice 10 Slab 2, Slice 5 Slab 2, Slice 10

FIGURE 6. (A) The direct inverse 3D FFT reconstruction of the fully-sampled 3D k-space of two simultaneously excited slabs using the traditional SMS pulse. (B) The results using the proposed SMSlab pulse with RF coding. The inter-slab aliasing artifacts are marked with yellow arrowheads. (C) The results using the proposed SMSlab pulse with RF encoding, together with NPEN correction for slab boundary artifacts. For clarity, in each slab, only one central and outer slice (slice 5 and 10) are displayed.

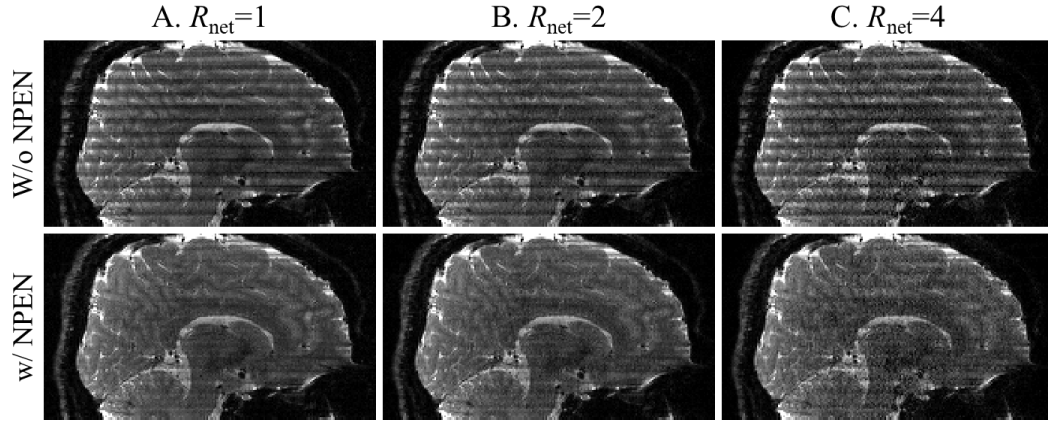


FIGURE 7. The reconstructed images of SMSlab acquisition at different net acceleration factors ($R_{\text{net}}=1, 2$ and 4), without and with NPEN correction. Images are shown in the sagittal view.

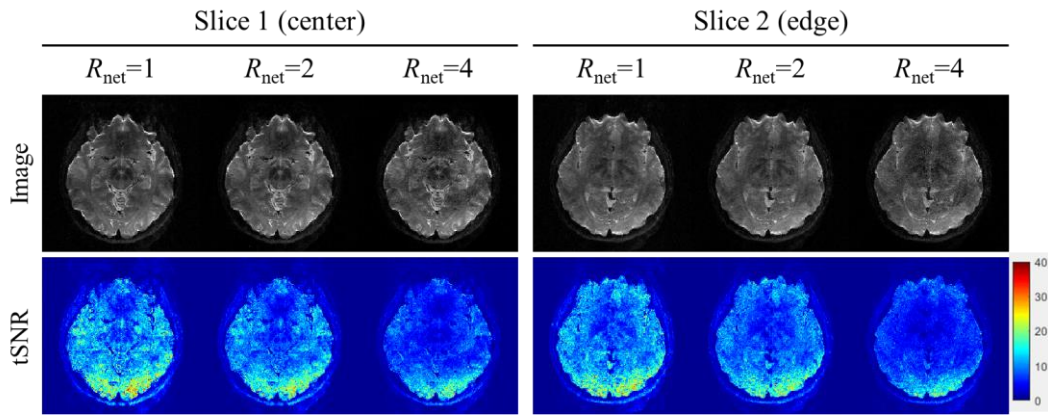


FIGURE 8. A comparison of the NPEN corrected images and tSNR maps at the slab center and edge. Three different SMSlab acquisitions are included: $R_{\text{net}}=1, 2$ and 4 . Only slight tSNR differences are observed between the slab center and edge.

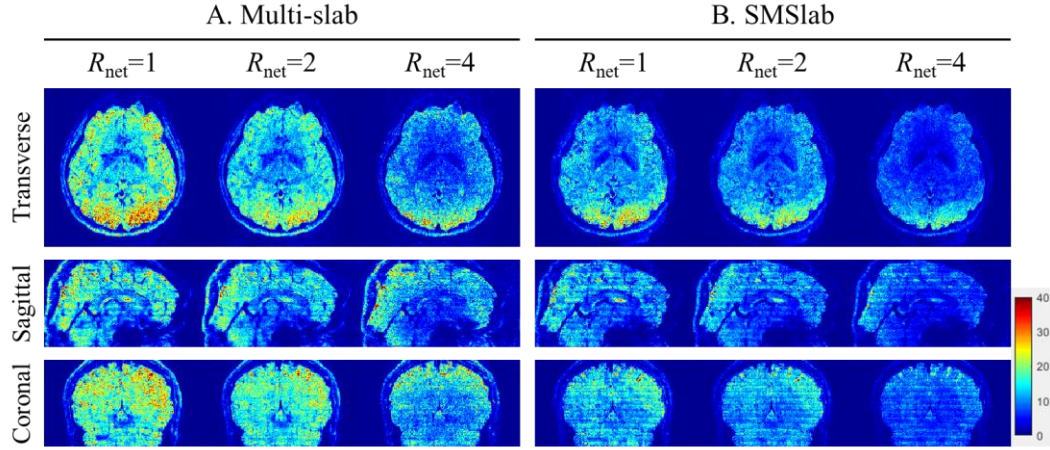


FIGURE 9. A comparison of tSNR maps between multi-slab (A) and SMSlab (B), at different net acceleration factors ($R_{\text{net}}=1, 2$ and 4), in the unequal TE case. The tSNR maps are shown from three different views.

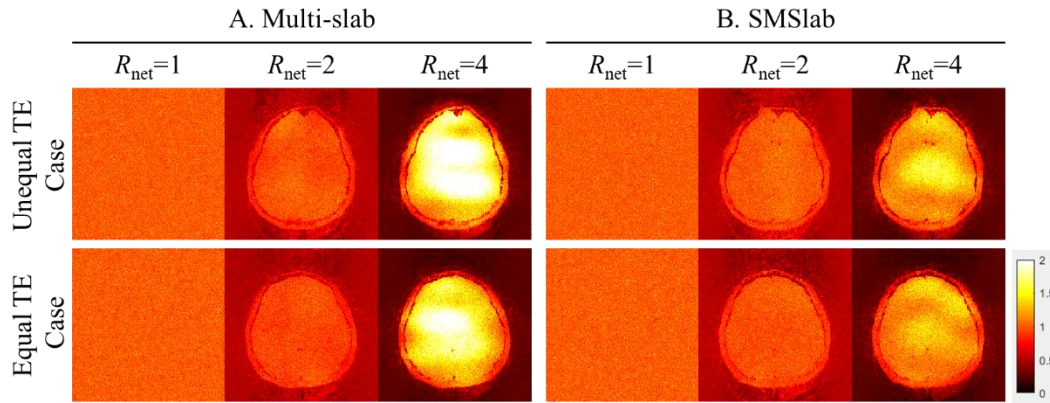
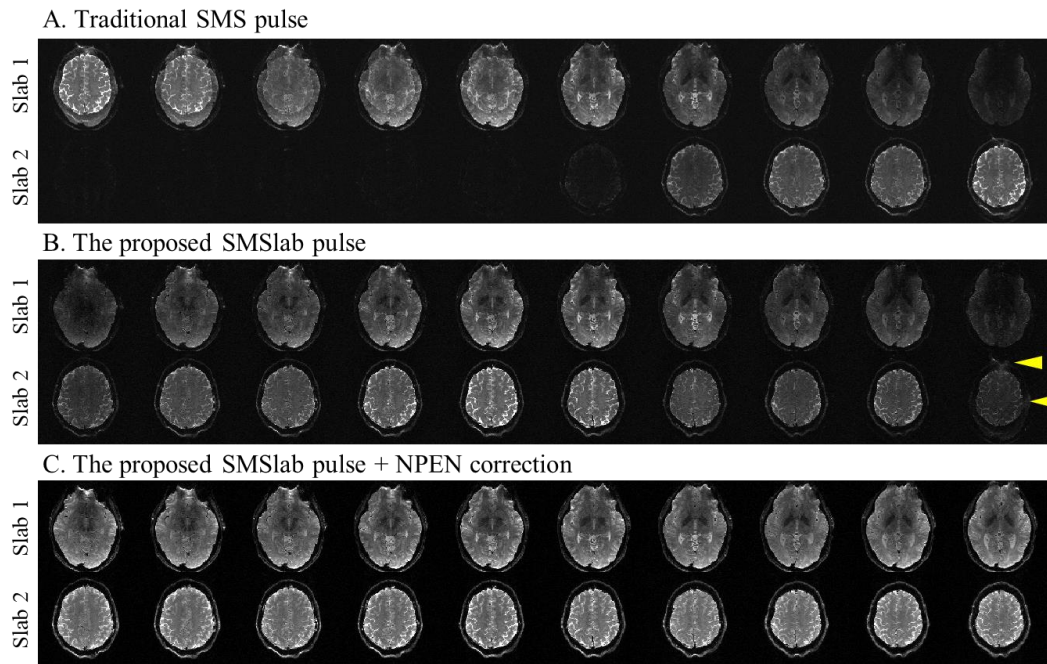


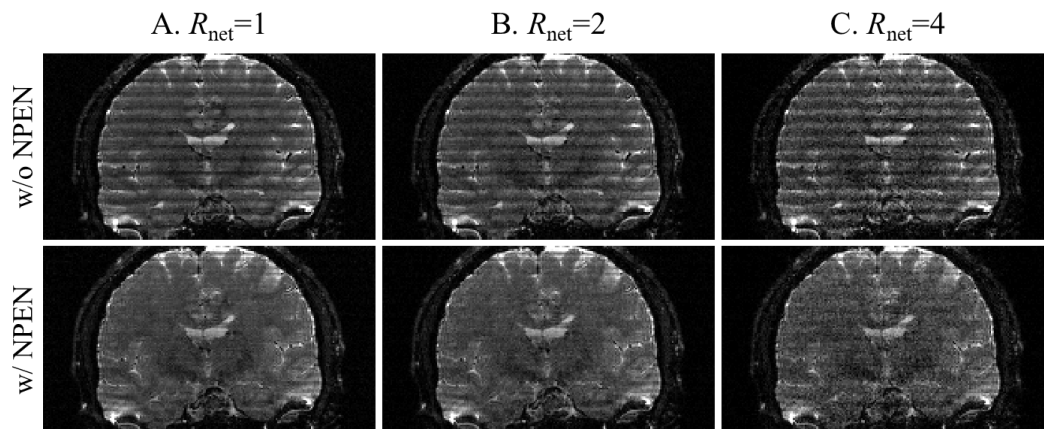
FIGURE 10. A comparison of g-factor maps between multi-slab (A) and SMSlab (B), in the unequal and equal TE cases. Results at three different net acceleration factors ($R_{\text{net}}=1, 2$ and 4) are compared. Only the central slice of a slab is shown for comparison.

Supporting Information

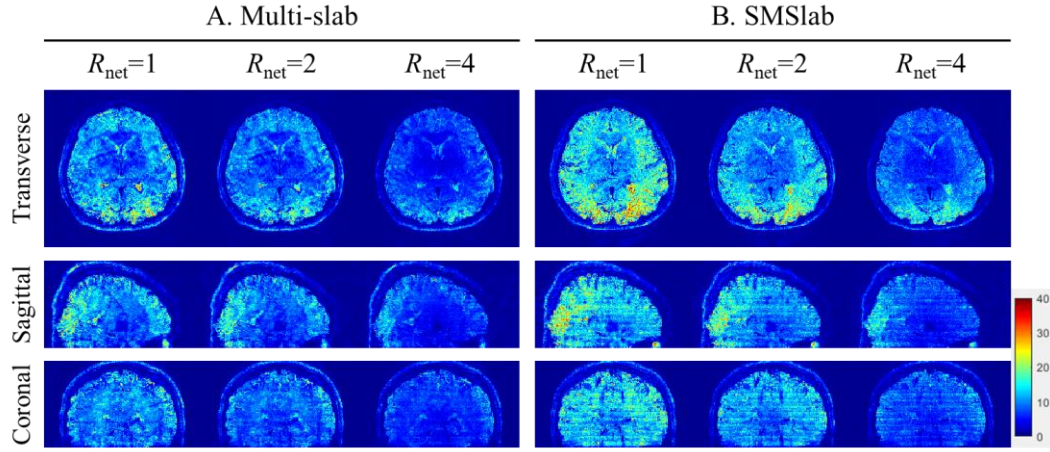
Figures



Supporting Information Figure S1. The full image set of the results in Figure 6. (A) The direct inverse 3D FFT reconstruction of the fully-sampled 3D k-space of two simultaneously excited slabs using the traditional SMS pulse. (B) The results using the proposed SMSlab pulse with RF coding. The inter-slab aliasing artifacts are marked with yellow arrowheads. (C) The results using the proposed SMSlab pulse with RF encoding, together with NPEN correction for slab boundary artifacts.



Supporting Information Figure S2. The reconstructed images of SMSlab acquisition at different net acceleration factors ($R_{\text{net}}=1, 2$ and 4), without and with NPEN correction. Images are shown in the coronal view.



Supporting Information Figure S3. A comparison of tSNR maps between multi-slab (A) and SMSlab (B), at different net acceleration factors ($R_{\text{net}}=1, 2$ and 4), in the equal TE case. The tSNR maps are shown from three different views.